ACS PHYSICAL CHEMISTRY Au
AN OPEN ACCESS JOURNAL OF THE AMERICAN CHEMICAL SOCIETY

pubs.acs.org/physchemau
Article

High Stability, Piezoelectric Response, and Promising Photocatalytic Activity on the New Pentagonal $CGeP_4$ Monolayer

José A. S. Laranjeira, Nicolas Martins, Pablo A. Denis, and Julio Sambrano*

Cite This: ACS Phys. Chem Au 2025, 5, 62−71
Read Online

ACCESS | Metrics & More | Article Recommendations | Supporting Information

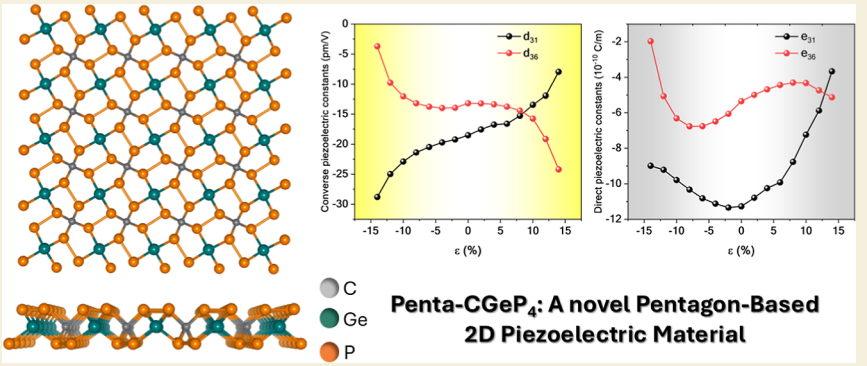

ABSTRACT: This study introduces the penta-structured semiconductor p-$CGeP_4$ through density functional theory simulations, which possesses an indirect band gap transition of 3.20 eV. Mechanical analysis confirms the mechanical stability of p-$CGeP_4$, satisfying Born−Huang criteria. Notably, p-$CGeP_4$ has significant direct (e_{31} = −11.27 and e_{36} = −5.34 × 10^{-10} C/m) and converse (d_{31} = −18.52 and d_{36} = −13.18 pm/V) piezoelectric coefficients, surpassing other pentagon-based structures. Under tensile strain, the band gap energy increases to 3.31 eV at 4% strain, then decreases smoothly to 1.97 eV at maximum stretching, representing an ∼38% variation. Under compressive strain, the band gap decreases almost linearly to 2.65 eV at −8% strain and then drops sharply to 0.97 eV, an ∼69% variation. Strongly basic conditions result in a promising band alignment for the new p-$CGeP_4$ monolayer. This suggests potential photocatalytic behavior across all tensile strain regimes and significant compression levels (ε = 0% to −8%). This study highlights the potential of p-$CGeP_4$ for groundbreaking applications in nanoelectronic devices and materials engineering.

KEYWORDS: *penta-graphene, piezoelectricity, $CGeP_4$, graphene, 2D material*

1. INTRODUCTION

The prediction of penta-graphene, also called p-CCC, in 2015 has added a new member to the extensive family of promising two-dimensional (2D) carbon allotropes.[1] p-CCC has an outstanding negative Poisson's ratio (NPR), which characterizes it as an auxetic nanomaterial with piezoelectricity and interesting optical properties.[2] The Cairo-type tessellation recognizes the building blocks of p-CCC with two out-plane distorted pentagons, which breaks the π-conjugation in this 2D material.[3] Studies suggest that the p-CCC structure can be obtained by employing chemical exfoliation using T12-carbon via dehydrogenation mechanism.[4] Additionally, the isolation of C_{20} fullerene also helps the synthesis availability of p-CCC in view of its composition by 12 pentagonal rings inside the cage.[5]

The intriguing pattern of p-CCC has motivated the research on pentagonal-based inorganic structures. In this sense, unitary pentagonal-based sheets such as penta-silicene and penta-germanene emerged with significant ferroelectricity and low thermal conductivity.[6] Extending for binary pentagon-based structures, p-CN_2,[7] p-BC_2,[8] p-SiC_2,[9] p-NiN_2,[3] and p-$PdSe_2$[10] are examples of stable compounds. Qu et al.[11] also evaluated the intrinsic photocatalytic application of 9 transition-metal MX_2 (M = Ni, Pd, and Pt, and X = S, Se, and Te) pentagon-based monolayers motivated by the synthesis of p-$PdSe_2$, which was obtained by micromechanical exfoliation of the bulk crystals.[10]

Recently, the proposition of ternary 2D pentagon-based structures has aroused the interest of many researchers, resulting in new applications and distinct properties.[12] For instance, p-BCN has intrinsic piezoelectricity and spontaneous polarization, which is significantly superior to the hexagonal boron nitride (h-BN) sheet.[13] Furthermore, the p-BNSi

Received: August 12, 2024
Revised: November 22, 2024
Accepted: November 22, 2024
Published: December 4, 2024

https://doi.org/10.1021/acsphyschemau.4c00068
ACS Phys. Chem Au 2025, 5, 62−71

predicted by Varjovi and colleagues[14] possesses a high level of exciton binding and strong light absorption in the visible region. A semiconductor behavior is verified in the recently proposed p-$SiXY_4$ (X = Si, C, Ge; Y = C, B, N), which reveals suitable band edge alignment for photocatalytic water splitting.[15] The NPR observed in p-CCC also emerges for the p-SiCN structure, whose monolayer is tunable under strain in terms of geometry (buckled-to-planar transition) and mechanical properties.[16]

Strain engineering has proven to be an effective strategy for tuning the electronic and mechanical properties of 2D pentagon-based materials. Applying biaxial strain on the p-BCN, Dabsamut and co-workers[17] have found a narrow band gap variation from 1.77 to 1.36 eV. Guo and Wang unveiled that[18] a compressive biaxial strain of 2% can slightly increase the piezoelectric coefficients of p-CCC by 3.1%. Liu et al.[19] showed that a small uniaxial strain to the p-BP_5 monolayer can shift its band gap from quasi-direct to direct, while a moderate biaxial strain can transform the p-BP_5 into a metal. In-plane tensile or compressive strain can modulate the carrier transport on p-SiC_2.[20] A uniaxial compressive strain of −8% along the *a*-direction significantly boosts the hole mobility along the *b*-direction by nearly 3 orders of magnitude, reaching 1.14×10^6 $cm^2\ V^{-1}\ s^{-1}$.

In view of the above-mentioned, this work aims to introduce p-$CGeP_4$ via density functional theory (DFT) simulations. A detailed study of its electronic, structural, mechanical, and vibrational properties was performed to characterize this new structure. Considering the potentiality of strain engineering for modulating the properties of 2D structures, the effects of biaxial strain on the electronic and piezoelectric properties of p-$CGeP_4$ were studied. It is expected that this study can highlight the promise of p-$CGeP_4$ for groundbreaking applications in nanoelectronic devices and materials engineering.

2. COMPUTATIONAL METHODOLOGY

Computational simulations were carried out using the CRYSTAL17 package[21] and based on the DFT in conjunction with the WC1LYP hybrid functional, which is described by the following equation: $E_{XC}[\rho] = aE_{HF}^{X} + (1 - a)E_{DFT}^{X} + E_{DFT}^{C}$, where E_{HF}^{X} is the exchange Hartree−Fock (HF) functional, E_{DFT}^{X} is the WC exchange functional, E_{DFT}^{C} denotes the LYP correlation functional, and a represents the mixing of the nonlocal HF exchange with the WC exchange functional (a = 16%). The triple-ζ valence with polarization[22] basis set was used to describe the C, Ge, and P atomic centers. The same methodology was used in previous work.[9]

The precision of the infinite Coulomb and HF exchange series is controlled by five α_i parameters with i = 1, 2, 3, 4, and 5, where α_1 is the overlap, α_2 is the penetration for Coulomb integrals, α_3 is the overlap for HF exchange integrals, and α_4 and α_5 are the pseudo-overlaps (HF exchange series). The two-electron contributions are neglected when the overlap between atomic functions is lower than $10^{-\alpha_i}$. For the calculations, the five α_i parameters were set to 20, 20, 20, 20 and 40, respectively. The convergence criterion for the self-consistent field (SCF) is 10^{-6} au/cell, while for geometry optimization, it is 10^{-7} au/cell, and for elastic constant calculations, it is 10^{-8} au/cell. The optimization convergence was checked on the root-mean-square (RMS) and the absolute value of the largest component of both the gradients and estimated displacements. The convergence criteria employed in the optimization for RMS and the largest component for gradient were 0.00030 and 0.00045 au, and for displacement 0.00120 and 0.00180 au, respectively. The reciprocal space was sampled using Pack-Monkhorst and Gilat nets with sublattices and a shrinking factor of 8, resulting in 90 *k*-points in the irreductible Brillouin zone. The vibrational modes at the Γ point were evaluated using the numerical second derivatives of the total energies estimated with the coupled perturbed HF/Kohn−Sham algorithm.[23]

The quantum theory of atoms in molecules and crystals (QTAIMC)[24,25] was employed to characterize the nature of chemical bonds. This approach uses the electronic density ($\rho(r)$) at the bond critical points (BCPs) to obtain topological parameters, such as the Laplacian ($\nabla^2\rho(r)$), the potential energy density ($V(r)$), the kinetic energy density ($G(r)$), and the total electronic energy density ($H(r) = V(r) + G(r)$). These parameters can provide valuable information regarding the type of bond interaction: shared shell (covalent bonds) or closed electron (ionic bonds).

The elastic constants (C_{ij}) were calculated as the second derivative of the energy (E) concerning the strain component (ϵ_i and ϵ_j) according to the following expression

$$C_{ij} = \partial^2 E/\partial\epsilon_i\partial\epsilon_j \tag{1}$$

To analyze the anisotropic mechanical behavior of the structures presented herein, the orientation-dependent Young modulus $Y(\theta)$, Poisson ratio $\nu(\theta)$, and shear modulus $G(\theta)$ were calculated employing the following expressions[26]

$$1/E(\theta) = S_{11}c^4 + S_{22}s^4 + 2S_{16}c^3s + 2S_{26}cs^3 + (S_{66} + 2S_{12})c^2s^2 \tag{2}$$

$$\nu(\theta)/E(\theta) = (S_{66} - S_{11} - S_{22})c^2s^2 - S_{12}(c^4 + s^4) + (S_{26} - S_{16})(cs^3 - c^3s) \tag{3}$$

$$1/4G(\theta) = (S_{11} + S_{22} - 2S_{12})c^2s^2 + S_{66}(c^2 - s^2)^2/4 - (S_{16} - S_{26})(c^3s - cs^3) \tag{4}$$

where $s = \sin\theta$, $c = \cos\theta$, and $\theta \in [0, 2\pi]$ is the angle with respect to the $+x$ axis. $S_{ij} = C_{ij}^{-1}$ is the elastic compliance constants.

The following equation calculated the direct (stress) piezoelectric constants $e_{ij} = |e|/2\pi V \cdot \sum_l (a_{ij} \cdot \partial\varphi_l/\partial\eta_v)$, where $|e|$ is the elementary charge, a_{ij} is the Cartesian component of the direct lattice basis vector, φ_l is the local function obtained utilizing the Berry phase approach, and η_v is the pure strain tensor.

Utilizing the Voigt notation for 2D materials and considering only in-plane strain components, the converse (strain) piezoelectric constant (d_{ij}) was obtained through the following relation

$$\begin{pmatrix} e_{11} & e_{12} & e_{16} \\ e_{21} & e_{22} & e_{26} \\ e_{31} & e_{32} & e_{36} \end{pmatrix} = \begin{pmatrix} d_{11} & d_{12} & d_{16} \\ d_{21} & d_{22} & d_{26} \\ d_{31} & d_{32} & d_{36} \end{pmatrix} \begin{pmatrix} C_{11} & C_{12} & C_{16} \\ C_{21} & C_{22} & C_{26} \\ C_{61} & C_{62} & C_{66} \end{pmatrix} \tag{5}$$

The thermodynamic stability of p-$CGeP_4$ was assessed by computing its cohesive energy (E_{coh}), which is defined by

$$E_{coh} = (E_{CGeP_2} - \sum_i n_i E_i)/\sum_i n_i \tag{6}$$

https://doi.org/10.1021/acsphyschemau.4c00068
ACS Phys. Chem Au 2025, 5, 62−71

where E_{CGeP_2} is the total energy of the p-$CGeP_4$ structure, E_i is the energy of an isolated atom i (C, Ge, P), and n_i is the number of i atoms in the sheet. By this definition, a negative value indicates an energetically stable material.

Molecular dynamics (MD) simulations were carried out using the extended tight-binding approximation (xTB)[27] as implemented in the DFTB$^+$ package,[28] with the GFN1-xTB parametrization.[29] The thermal stability of p-$CGeP_4$ was studied using the Berendsen thermostat[30] at 300 K by 40 ps with a time step of 1 fs. In the next step, MD simulations were conducted, starting at 300 K and continuing until structural rupture.

3. RESULTS AND DISCUSSION

3.1. Structure and Stability

The novel pentagonal-based $CGeP_4$ structure belongs to the space group $P\bar{4}$ (no. 81) with a square symmetry, with lattice parameters $a = b = 4.58$ Å. As can be seen in Figure 1a, each

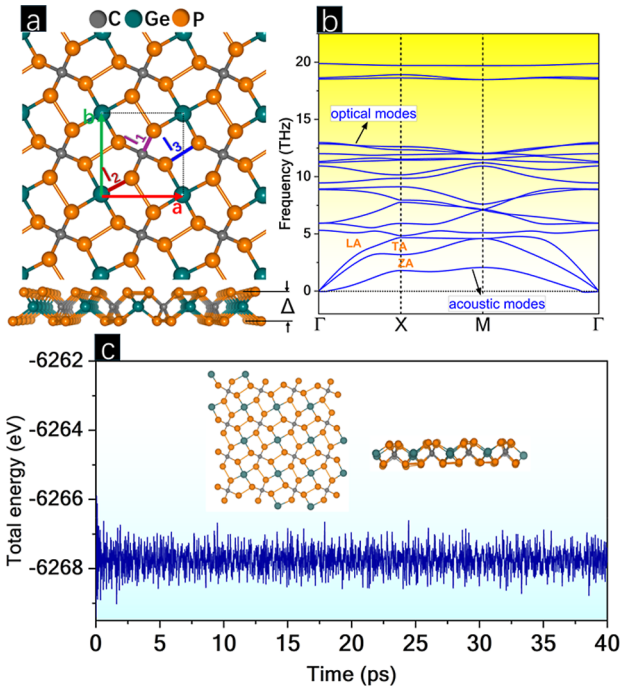

Figure 1. (a) p-$CGeP_4$ lattice with unit cell and their three nonequivalent bonds highlighted, (b) phonon bands dispersion, and (c) MD simulation at 300 K of p-$CGeP_4$ along with last iteration snapshot.

unit cell of p-$CGeP_4$ consists of carbon and germanium atoms, each 4-fold coordinated with phosphorus. The unit cell comprises three non-equivalent atoms with internal coordinates Ge (0.000, 0.000, 0.000), C (0.500, 0.500, 0.000), and P (0.634, 0.792, 0.064). The optimized p-$CGeP_4$ has a buckling height (Δ) of 2.56 Å, superior to the p-CCC (Δ = 1.22 Å) and other ternary compounds like p-BCN (Δ = 1.37 Å) and p-CNP (Δ = 2.43 Å), all obtained at the DFT/WC1LYP level. In this pentagonal lattice, the l_1 (C−P), l_2 (Ge−P), and l_3 (P−P) bond lengths are 1.95, 2.31, and 2.28 Å, respectively, values that support its higher thickness. The thermodynamic stability of p-$CGeP_4$ was calculated via E_{coh}, and a value of −4.17 eV/atom was obtained, which is comparable to those obtained for well-reported monolayers, such as p-CCC (−6.83 eV/atom), p-BCN (−6.38 eV/atom), and p-CNP (−5.12 eV/atom).

The phonon bands dispersion is an important tool to certify the dynamic stability of 2D materials.[31] Clearly, as presented in Figure 1b, the vibrational bands of p-$CGeP_4$ do not have regions with imaginary frequencies, therefore indicating that p-$CGeP_4$ is a free-standing monolayer. Additionally, the phonon dispersion curves of p-$CGeP_4$ comprise 3 acoustic and 15 optical modes, which relate to the in-phase and out-phase vibrations, respectively. The acoustic branches can be attributed to the longitudinal acoustic mode (LA), transversal acoustic mode (TA) and out-of-plane acoustic mode (ZA), whose frequencies are 4.68, 4.58, and 2.06 THz around the M point, respectively, except for LA mode that occurs at X point. On the other hand, the highest optical mode occurs at 19.87 THz in the center of the Brillouin zone (Γ point). An absence of intersections or overlaps between the acoustic modes or between the acoustic and optical modes is noticed, indicating low phonon scattering channels. The thermal stability of the p-$CGeP_4$ at room temperature (300 K) was verified by MD simulations, and the variation of the total energy as a function of the simulation time (40 ps) can be visualized in Figure 1c. Our dynamics suggest a small energy fluctuation and the absence of significant lattice distortion on the p-$CGeP_4$ geometry, attesting to its feasibility. As detailed in the Supporting Information, the p-$CGeP_4$ monolayer demonstrates impressive thermal stability, withstanding temperatures up to approximately 2050 K without experiencing ruptures or reconstructions.

3.2. Electronic Description

The band structure and density of states (DOS) are listed in Figure 2. The band structure reveals an indirect band gap

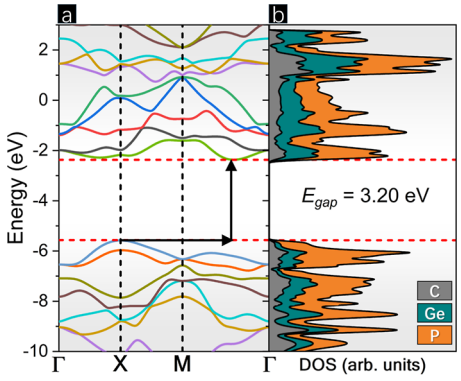

Figure 2. (a) Band structure and (b) density of states (DOS) for p-$CGeP_4$.

transition of 3.20 eV, with the valence band maximum (VBM) at the X point and the conduction band minimum (CBM) between the M and Γ points. The DOS shows a higher density of P states compared to Ge and C states along the valence and conduction bands, respectively. In the VBM, the DOS shows a softer behavior compared to the CBM, indicating higher band dispersion and, therefore, higher mobility of photogenerated holes. The similarity between the shapes of the DOS curves for all atoms reveals strongly correlated states in p-$CGeP_4$.

The QTAIMC analysis was utilized to access the chemical character of the l_1, l_2, and l_3 nonequivalent bonds of p-$CGeP_4$. The electronic density topological parameters are listed in Table 1.

https://doi.org/10.1021/acsphyschemau.4c00068
ACS Phys. Chem Au 2025, 5, 62−71

Table 1. Topological Parameters Based on the QTAIMC Analysis for l_1, l_2, and l_3 Bonds in p-$CGeP_4$, Where $\rho(r)$ is the Charge Density, $\nabla^2\rho(r)$ is the Laplacian of the Charge Density, $|V(r)|/G(r)$ is the Ratio Between the Virial $V(r)$ and the Kinetic Density Energy $G(r)$, $H(r)/\rho(r)$, and $G/\rho(r)$

bond	$\rho(r)$	$\nabla^2\rho(r)$	$\lvert V(r)\rvert/G(r)$	$H(r)/\rho(r)$	$G/\rho(r)$
l_1 (C−P)	0.128	−0.043	2.332	−0.340	0.340
l_2 (Ge−P)	0.094	−0.111	3.154	−0.231	0.231
l_3 (P−P)	0.104	−0.183	2.871	−0.408	0.408

Espinosa et al.[32] classify the bonds based on the $|V(r)|/G(r)$ ratio at the BCPs. For closed-shell interactions, such as ionic bonds, we have $|V(r)|/G(r) < 1$, while open-shell interactions are expected to have $|V(r)|/G(r) > 2$. Values between 1 and 2 indicate a transitory region, where there is an early stage of covalent bond formation. Macchi et al.[33] propose that $H/\rho(r) > 0$, and $G/\rho(r) > 1$ characterize closed-shell interactions. On the other hand, open-shell interactions are expected to have $H/\rho(r) < 0$, and $G/\rho(r) < 1$. As suggested by the DOS curves, the bonds are strongly covalent, i.e., possess higher closed-shell character due to its $\nabla^2\rho(r) < 0$, $|V(r)|/G(r) > 2$, and $H/\rho(r) < 0$. The l_3 (P−P) and l_2 (Ge−P) present the highest covalent character and $|V(r)|/G(r)$ ratio, respectively.

3.3. Mechanical Properties

Table 2 shows the mechanical properties of p-$CGeP_4$ and other pentagon-based monolayers. For square lattices, the Born−Huang criteria[34] is described by $C_{11} > 0$, $C_{66} > 0$, and $C_{11} > |C_{12}|$, which is fulfilled, confirming the mechanical stability of p-$CGeP_4$. p-$CGeP_4$ exhibits maximum and minimum Young modulus (Y_{max} and Y_{min}) of 100.23 and 77.58 N/m, Poisson Ratio (ν_{max} and ν_{min}) of 0.26 and 0.03, and shear modulus (G_{max} and G_{min}) of 48.55 and 31.01 N/m, respectively. Notice that C_{11}, C_{22}, C_{12}, C_{66}, G_{max}/G_{min}, and Y_{max}/Y_{min} are significantly lower than the values exhibited for the other penta-graphene-like structures. About the ν_{max}/ν_{min}, p-$CGeP_4$ does not present a negative Poisson ratio as the other structures. Furthermore, p-$CGeP_4$ has a remarkable anisotropy for this parameter, a feature not observed for the other monolayers. Differently from other ternary pentagon structures, p-$CGeP_4$ has $C_{11} = C_{22}$. This means that the combination of different species at the cation (sp^3-site) results in a disorder lower than that in the anion site (sp^2-site), which is corroborated by the fact that the p-CNP and p-BCP show rectangular lattices. At the same time, the p-$CGeP_4$ remains with square symmetry as the p-CCC.

The polar representations of Y, ν, and G were adopted to analyze the anisotropy for p-$CGeP_4$, as represented in Figure 3. It can be noticed that the anisotropy is more remarkable for ν. A distinctive characteristic of p-$CGeP_4$ is their closer to zero ν at approximately $k\pi/4$ (k as an integer) angles, which indicates that for this orientation, the material does not change in lateral dimensions when stretched or compressed. The Y and G show a square-like shape with maximum values for angles closer to $k\pi/3$ and $k\pi/4$, respectively.

Due to their asymmetric crystalline structure, some materials can exhibit piezoelectricity, which allows them to generate polarization in response to mechanical stress or strain. The P-$CGeP_4$ lattice only comprises the identity and three 2-fold rotation axes, not presenting an inversion center; i.e., it is a non-centrosymmetric structure, which gives it the ability to exhibit piezoelectricity.[35] In view of this, the piezoelectric stress (e_{ij}) and strain (d_{ij}) constants of p-$CGeP_4$ and other pentagon-based monolayers[9,17,18,36,37] are represented in Table 3. It can be noticed that p-$CGeP_4$ exhibits non-null direct ($e_{31} = -11.27$ and $e_{36} = -5.34 \times 10^{-10}$ C/m) and converse ($d_{31} = -18.52$ and $d_{36} = -13.18$ pm/V) piezoelectric coefficients, which are significantly higher than those obtained at the theory level for another pentagon-based structure, which makes this compound promising for advanced applications such as sensors, actuators, energy harvesting, and consumer electronics.

3.4. Vibrational Analysis

Vibrational analysis was utilized to analyze the short-range order in p-$CGeP_4$. The Raman and IR spectra are shown in Figure 4. The presence of 18 active modes $\Gamma_{vib} = 3A + 5B + 10E$ was verified to be all Raman-active and $\Gamma_{IR} = A + 5B + 10E$ to be IR-active. Three main peaks observed in the Raman spectrum were at 374.26, 401.16, and 432.57 cm^{-1}, with E, B, and B symmetries, respectively. At 374.26 cm^{-1}, two doubly degenerate modes were noted, and the symmetric stretching of Ge−P bonds characterized the motion. For 401.16 cm^{-1}, scissoring was noted, with the motion occurring due to the displacement of P atoms. In 432.57 cm^{-1}, asymmetrical stretching was observed for the C−P and Ge−P bonds. Regarding the IR spectrum, the three most intense peaks occurred at 295.97, 374.26, and 619.18 cm^{-1}, all being E doubly degenerate modes, i.e., each possessing two associated vibrations. At 295.97 and 619.18 cm^{-1}, the vibrations were associated with the asymmetric stretching of the C−P bonds.

3.5. Strain Engineering

Here, the homogeneous biaxial strain (ε) is applied on the p-$CGeP_4$ in both compressive and tensile regimes, following the relation $\varepsilon = (a - a_0)/a_0$, where the strained and unstrained lattice parameters are represented by a and a_0, respectively. Our simulations suggest p-$CGeP_4$ stability under a −14% to +14% range of biaxial strain. As a first analysis, the changes in the bond lengths induced by the strain deformation were assessed, as seen in Figure 5a. Under tensile strain, the out-of-

Table 2. Calculated Elastic Constants C_{11}, C_{12}, and C_{66} (N/m), Maximum and Minimum Values of Young Modulus (Y_{max}/Y_{min}) (N/m), Poisson Ratio (ν_{max}/ν_{min}), and Shear Modulus (G_{max}/G_{min}) (N/m) for p-$CGeP_2$, and Other Pentagon-Based Monolayers Obtained at WC1LYP/DFT Level

	C_{11}	C_{22}	C_{12}	C_{66}	Y_{max}/Y_{min}	ν_{max}/ν_{min}	G_{max}/G_{min}
p-$CGeP_4$	83.22	83.22	20.36	48.12	100.23/77.58	0.26/0.03	48.55/31.01
p-SiC_2	151.52	151.52	6.26	82.46	161.27/151.27	0.04/−0.02	82.46/72.63
p-GeC_2	136.50	136.50	7.65	72.72	144.80/136.07	0.08/−0.01	72.72/64.43
p-CNP	194.26	185.90	10.66	106.63	207.09/185.31	0.06/−0.03	106.63/89.67
p-BCN	187.21	229.18	7.46	114.51	230.11/186.97	0.03/−0.04	114.51/99.35
p-CCC	281.17	281.17	−22.49	160.39	286.40/279.38	−0.08/−0.11	160.39/151.83

https://doi.org/10.1021/acsphyschemau.4c00068
ACS Phys. Chem Au 2025, 5, 62−71

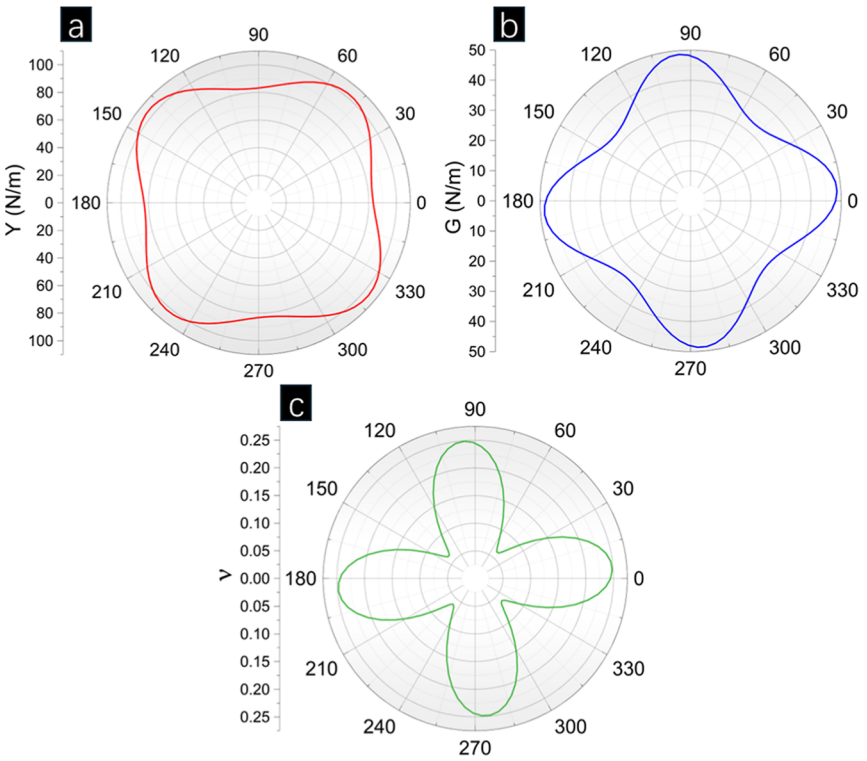

Figure 3. Representation of the angular dependence of (a) Young modulus (Y), (b) shear modulus (G), and (c) Poisson ratio (ν) for p-$CGeP_4$.

Table 3. Piezoelectric Stress (e_{ij}) (10^{-10} C/m) and Strain (d_{ij}) (pm/V) Constants of p-$CGeP_4$ Monolayer Compared to Other Pentagonal-Based Structures (p-SiC_2, p-GeC_2, p-CNP, p-BCN, and p-CCC). All results were obtained at DFT/WC1LYP level.

system	e_{11}	e_{12}	e_{31}	e_{36}	d_{11}	d_{12}	d_{31}	d_{36}
p-$CGeP_4$			−11.27	−5.34			−18.52	−13.18
p-SiC_2				−0.61				−0.74
p-GeC_2				−1.59				−2.20
p-CNP	−2.37	−0.44		−0.73	−1.22	−0.17		−0.69
p-BCN	−2.43	−1.40		1.29	−1.28	−0.56		1.13
p-CCC				−0.03				−0.02

plane bond lengths l_1 (C−P) and l_2 (Ge−P) increase, changing from 1.96 to 2.07 Å (l_1) and 2.31 to 2.51 Å (l_2) at maximum stretching (ε = +14%). Meanwhile, a small effect of this positive strain on the in-plane l_3 (P−P) bond length is registered, and the 2.31 Å value found at ε = +6% is maintained until +14% of strain, which is closer to that noticed in the strain-free state (2.28 Å). Thus, this behavior suggests a minor push strength effect on the P−P bond. On the other hand, the compressive regime acts noticeably in the Ge−P bond, modifying it to 2.18 Å (ε = −14%), being slightly smaller than those found at the same level of compression for P−P bond length (2.19 Å). Therefore, the maximum compression rearranges the bond length order observed at equilibrium (ε = 0%), i.e., $l_2 > l_3 > l_1$ to $l_3 > l_2 > l_1$.

The trend mentioned above can be related to the strain effect on the buckling height of p-$CGeP_4$, which was plotted in Figure 5b. As the tension increases, the Δ parameter of 2.56 Å is mitigated to 2.28 Å when ε = +14% is applied, which favors the increment on the out-of-plane bonds, C−P and Ge−P. Oppositely, the compression induces a thickness enlargement, and Δ = 2.89 Å is found for ε = −14%. Our results met those reported for other pentagonal-based lattices, such as B_2C,[8] SiCN,[16] and PBN,[38] revealing stretching as a crucial factor in reducing the monolayer thickness.

In this work, the band gap variation of p-$CGeP_4$ in the function of the biaxial strain is also analyzed, as noted in Figure 5b. Under the tensile regime, the E_{gap} grows up to 3.31 eV at 4% strain and then is smoothly reduced at the value of E_{gap} = 1.97 eV for maximum stretching, representing an ∼38% decrease compared to the band gap at equilibrium (E_{gap} = 3.20 eV). On the other hand, the negative strain decreases the band gap almost regularly until ε = −8%, with E_{gap} = 2.65 eV, whose value drops significantly to 0.97 eV at the maximum level of compression and denotes a variation of ∼69%. Using the HSE06 level, Li and co-workers[8] appoint that p-B_2C, E_{gap} = 2.47 eV, has its band gap decreased to 2.21 (1.83 eV) when 10% of compressive (tensile) strain is applied. The same trend occurs for p-PtSiTe, where the band gap of 0.80 eV (strain-free state) is tuned to ∼0.30 and 0.65 eV at ε = −10 (10%).[39] P-BP_5,[38] p-Sb_2Si,[40] and P_2C[41] are some pentagonal sheets that present a similar band gap reduction by strain effect.

In general, in semiconductors with distinct ring circuits, such as tetragonal BN,[42] SiC,[43] and InN-based[44] graphenylenes or GeC[45] and ZnS[46] honeycomb lattices, the compressive regime increases the band gap of the material. Here, both negative and positive deformations lead the p-$CGeP_4$ band gap to the visible-light range, a required condition for many semiconductor devices.

https://doi.org/10.1021/acsphyschemau.4c00068
ACS Phys. Chem Au 2025, 5, 62−71

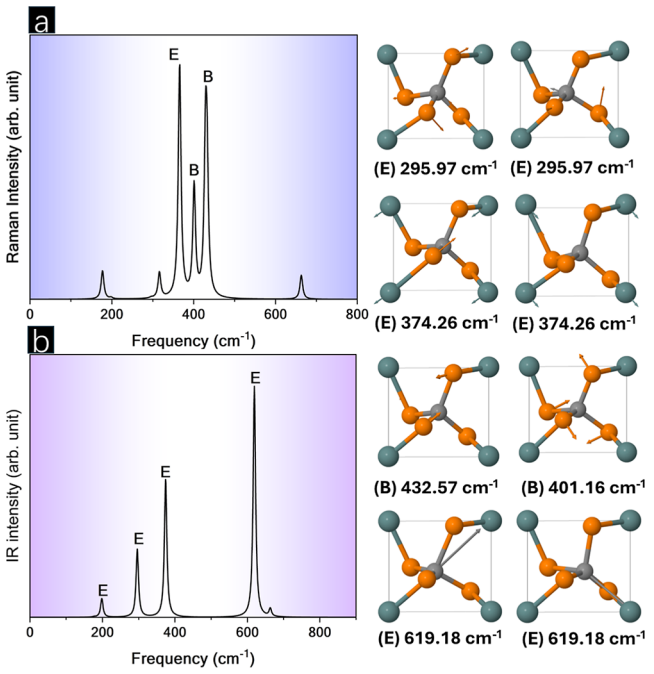

Figure 4. (a) Raman and (b) IR spectra along with the vibration associated with most intense peaks for both.

To take into account the piezoelectric response of p-$CGeP_4$ when affected by biaxial strain, Figure 6 denotes the variation of the e_{31}, e_{36}, d_{31}, and d_{36} coefficients. Both e_{31} and e_{36} coefficients decrease (in module) by tensile strain application and are equal to 3.66 and 5.12 × 10^{-10} C/m at maximum stretching, respectively (see Figure 6b). The same reduction occurs in negative strain for the e_{31} coefficient, whose value is found to be 8.69 × 10^{-10} C/m at maximum compression. On the contrary, the compression increases $|e_{36}|$ to 6.77 × 10^{-10} C/m when ε = −8% and then falls to 1.97 × 10^{-10} C/m (when ε = −14%). In addition to that, each of d_{31} and d_{36} components assume a distinct plot, as seen in Figure 6a. While $|d_{31}|$ increases from a strain-free state to the top level of compression, reaching 28.80 pm/V. The same coefficient becomes smaller as the stretching expands, and 7.95 pm/V is found. On the other hand, the $|d_{36}|$ of p-$CGeP_4$ is enhanced when tensile strain is applied, 24.21 pm/V at ε = 14%, and reduced under the compressive regime, 3.71 pm/V at ε = −14%. Investigating the g-C_3N_4 monolayer, Guo and colleagues[47] appoint a significant increase of 330% in the d_{11} coefficient comparing 4% of stretching with the equilibrium. Different to that reported here, Janus monolayers such as SbTeI and BiTeI do not have a strain-dependent d_{31} behavior, which suggests the huge importance of symmetry in this kind of property.[48] In general, the piezoelectric properties of p-$CGeP_4$ can be tuned by applying a selective strain range, and all coefficients maintain great values. As the p-$CGeP_4$ is still a semiconductor when deformed (see Figure 5b), it can perform a promising role as a novel piezoelectric 2D material under mechanical strain.

Among the many strategies to make a material suitable for photocatalytic processes, strain engineering is one of the most promising solutions. As expected, the semiconductor should have an appropriate band gap for a visible-light-driven photocatalyst (1.5 < E_{gap} < 3.0 eV).[49] By applying biaxial strain, this requirement can be achieved in p-$CGeP_4$, as seen in Figure 7b, where the band gap reaches the visible range of the spectrum (390−760 nm) to harvest solar power. Another favorable condition for the potential use of p-$CGeP_4$ as a photocatalyst is due to their indirect band gap feature since the electron−hole recombination is mitigated by the presence of distinct *K*-points between the VBM and CBM.[50] The principle of water splitting consists of the photoexcited electron−hole pair separation that is driven to the surface without any recombination. Then, the photogenerated electrons (e^-) reduce the water molecules into H_2: $2H^+ + 2e^- \rightarrow H_2$, and in the same way, the induced holes (h^+) oxidize H_2O into O_2: $H_2O + 2h^+ \rightarrow 1/2O_2 + 2H^+$.[51] Aiming at water splitting purposes, the CBM position should be more positive than the reduction potential (H^+/H_2), −4.44 eV at pH = 0, and the VBM position should be more negative than the oxidation potential (O_2/H_2O), −5.67 eV at pH = 0.[52]

Here, the band alignment of p-$CGeP_4$ is assessed under the biaxial strain effect and considering different pH conditions by using the equations[53]

$$E^{red}_{H^+/H_2} = -4.44 + 0.059 \times pH \quad (7)$$

$$E^{ox}_{O_2/H_2O} = -5.67 + 0.059 \times pH \quad (8)$$

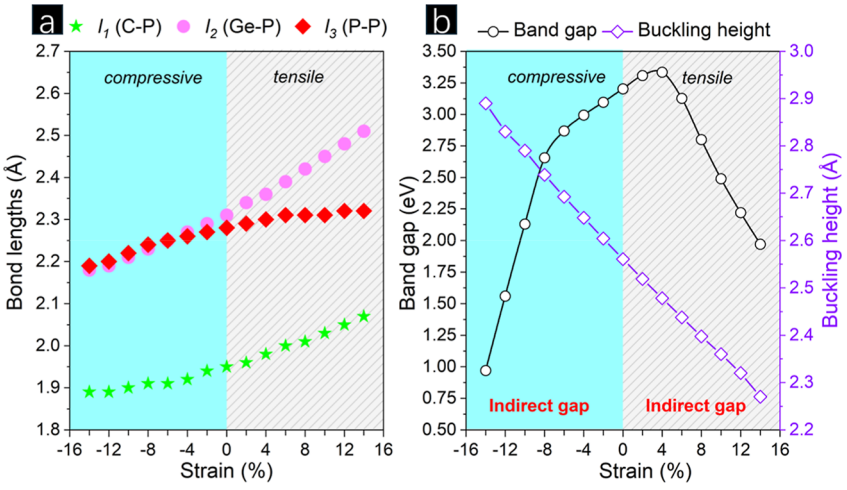

Figure 5. (a) Bond lengths and (b) band gap energy and buckling as a function of biaxial strain.

https://doi.org/10.1021/acsphyschemau.4c00068
ACS Phys. Chem Au 2025, 5, 62−71

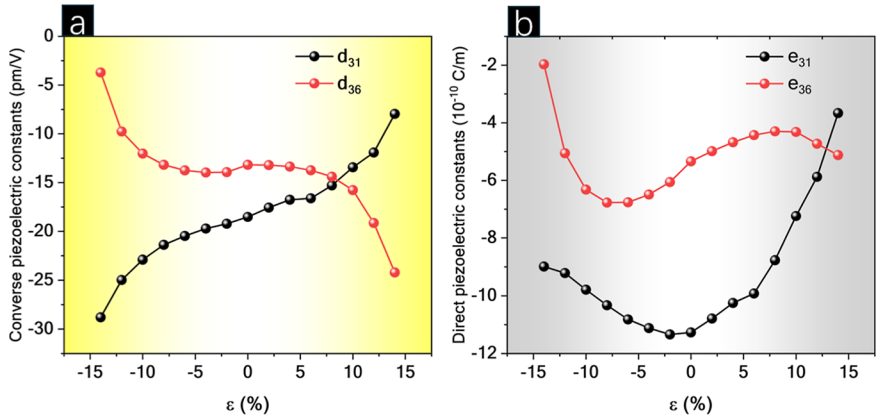

Figure 6. (a) Direct e_{31} and e_{36} and (b) converse d_{31} and d_{36} piezoelectric coefficients as a function of biaxial strain.

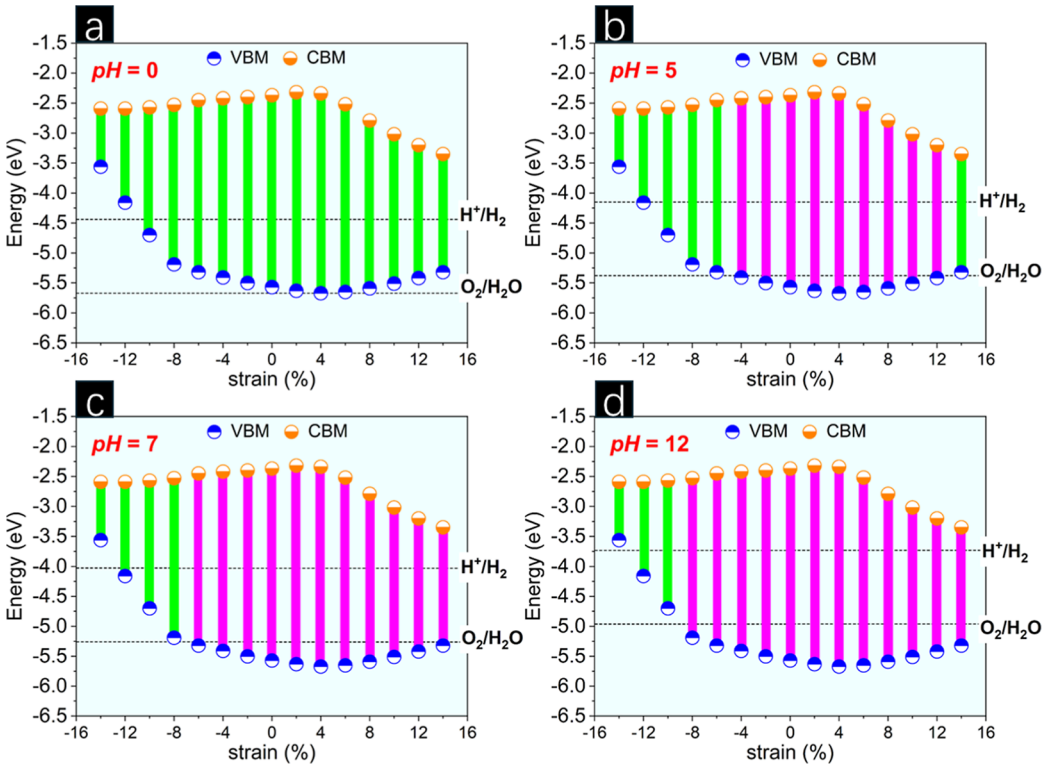

Figure 7. Band alignments of $CGeP_4$ monolayer under biaxial strain at pH equal to (a) 0, (b) 5, (c) 7, and (d) 12.

In the vacuum (pH = 0), the unstrained and deformed p-$CGeP_4$ monolayer matches the H^+/H_2 potential (see Figure 7a). On the other hand, the VBM position of p-$CGeP_4$ under all strain applications, even in a strain-free state, appears above the O_2/H_2O potential, which does not meet the full requirements for water splitting. A usual strategy to tune the water redox potentials of a material to attend photocatalytic promises can be applying an external bias potential by changing the pH environment.[54] Therefore, Figure 7b–d denotes the band offsets when the photocatalytic surface is submitted to weakly acidic (pH = 5), neutral (pH = 7), and strongly basic conditions (pH = 12). Clearly, we can see a suitable band alignment at the acid environment for p-$CGeP_4$ at equilibrium, as well as at most levels of tension (ε = 0% to +12%) and determined values (ε = −2% and −4%) of compression. The p-$CGeP_4$ monolayer also sandwiches both H^+/H_2 and O_2/H_2O potentials for a neutral pH. Under pH = 7, the VBM position is also suitable for ε = +14% and ε = −6%, in addition to the appropriate region of strain mentioned in the acidic case. The strongly basic condition offers the most promising band alignment for the new p-$CGeP_4$ monolayer, making it a pentagonal structure with potential photocatalyst behavior for all tensile strain regimes and also under significant levels of compression (ε = 0% to −8%). Thus, considering strongly acidic and basic pH values, and also the neutral pH, the p-$CGeP_4$ substrates can promote photogenerated electrons and holes to drive the water-splitting reactions and could be useful as visible-light photocatalytic devices due to their suitable band gap under strain engineering.

4. CONCLUSIONS

A novel pentagonal $CGeP_4$ monolayer (p-$CGeP_4$) was unveiled, and its structural, electronic, vibrational, piezoelectric, and photocatalytic properties under biaxial strain

https://doi.org/10.1021/acsphyschemau.4c00068
ACS Phys. Chem Au 2025, 5, 62−71

were thoroughly examined by means of DFT simulations. The p-$CGeP_4$ monolayer is identified as an indirect wide band gap semiconductor (E_{gap} = 3.20 eV) with dynamic stability, evidenced by the absence of imaginary phonon modes and remarkable thermal stability up to approximately 2050 K. The mechanical analysis confirms the material stability, with Young modulus ranging between 77.58 and 100.23 N/m, Poisson ratio from 0.03 to 0.26, and shear modulus from 31.01 to 48.55 N/m. Notably, p-CGeP4 exhibits significant direct (e_{31} = −11.27 and e_{36} = -5.34×10^{-10} C/m^2) and converse (d_{31} = −18.52 and d_{36} = −13.18 pm/V) piezoelectric coefficients, surpassing other pentagon-based structures and indicating strong potential for applications in energy devices.

The monolayer can be homogeneously compressed or stretched up to −14% and +14% strain, respectively. Mechanical deformation significantly tunes its electronic structure with the band gap increasing to 3.31 eV under 4% tensile strain and decreasing to 1.97 eV at maximum stretching. In comparison, compressive strain reduces the band gap to 2.65 eV at −8% and further to 0.97 eV. Band edge alignment analysis shows that strongly basic conditions offer the most promising band alignment for the new p-$CGeP_4$ monolayer, with potential photocatalytic behavior across all tensile strain regimes and significant compression levels (ε = 0% to −8%). The p-$CGeP_4$ shows promising material applications in nanoelectronics, energy devices, and materials engineering, offering new perspectives for photocatalytic devices under stress conditions.

■ ASSOCIATED CONTENT

Supporting Information

The Supporting Information is available free of charge at https://pubs.acs.org/doi/10.1021/acsphyschemau.4c00068.

MD simulation for stability at 300 K by 40 ps (MP4)

MD simulation of heating from 300 K up to rupture (MP4)

■ AUTHOR INFORMATION

Corresponding Author

Julio Sambrano − *Modeling and Molecular Simulation Group, São Paulo State University (UNESP), School of Sciences, Bauru 17033-360, Brazil;* orcid.org/0000-0002-5217-7145; Email: jr.sambrano@unesp.br

Authors

José A. S. Laranjeira − *Modeling and Molecular Simulation Group, São Paulo State University (UNESP), School of Sciences, Bauru 17033-360, Brazil;* orcid.org/0000-0002-8366-7227

Nicolas Martins − *Modeling and Molecular Simulation Group, São Paulo State University (UNESP), School of Sciences, Bauru 17033-360, Brazil*

Pablo A. Denis − *Computational Nanotechnology, DETEMA, Facultad de Química, UDELAR, Montevideo 11800, Uruguay;* orcid.org/0000-0003-3739-5061

Complete contact information is available at: https://pubs.acs.org/10.1021/acsphyschemau.4c00068

Author Contributions

CRediT: **José Artigas dos Santos Laranjeira** conceptualization, data curation, formal analysis, investigation, methodology, writing - original draft, writing - review & editing; **Nicolas Martins** data curation, formal analysis, writing - original draft, writing - review & editing; **Pablo A. Denis** visualization, writing - review & editing; **Julio Ricardo Sambrano** funding acquisition, resources, supervision, validation, writing - review & editing.

Funding

The Article Processing Charge for the publication of this research was funded by the Coordination for the Improvement of Higher Education Personnel - CAPES (ROR identifier: 00x0ma614).

Notes

The authors declare no competing financial interest.

■ ACKNOWLEDGMENTS

This work was supported by the Brazilian funding agencies Fundação de Amparo à Pesquisa do Estado de São Paulo—FAPESP (grant nos. 22/03959-6, 22/00349-2, 22/14576-0, and 20/01144-0, 22/16509-9), National Council for Scientific and Technological Development—CNPq (grant no. 307213/2021-8), Coordination for the Improvement of Higher Education Personnel (grant no. 88887.827928/2023-00), and Uruguay funding agencies PEDECIBA Quimica, CSIC, and ANII. The computational facilities were supported by resources supplied by the Molecular Simulations Laboratory (São Paulo State University, Bauru, Brazil).

■ REFERENCES

(1) Zhang, S.; Zhou, J.; Wang, Q.; Chen, X.; Kawazoe, Y.; Jena, P. Penta-graphene: A new carbon allotrope. *Proc. Natl. Acad. Sci. U.S.A.* **2015**, *112*, 2372−2377.

(2) Nazir, M. A.; Hassan, A.; Shen, Y.; Wang, Q. Research progress on penta-graphene and its related materials: Properties and applications. *Nano Today* **2022**, *44*, 101501.

(3) Bykov, M.; Bykova, E.; Ponomareva, A. V.; Tasnádi, F.; Chariton, S.; Prakapenka, V. B.; Glazyrin, K.; Smith, J. S.; Mahmood, M. F.; Abrikosov, I. A.; Goncharov, A. F. Realization of an Ideal Cairo Tessellation in Nickel Diazenide NiN_2: High-Pressure Route to Pentagonal 2D Materials. *ACS Nano* **2021**, *15*, 13539−13546.

(4) Zhao, Z.; Tian, F.; Dong, X.; Li, Q.; Wang, Q.; Wang, H.; Zhong, X.; Xu, B.; Yu, D.; He, J.; Wang, H.-T.; Ma, Y.; Tian, Y. Tetragonal Allotrope of Group 14 Elements. *J. Am. Chem. Soc.* **2012**, *134*, 12362−12365.

(5) Prinzbach, H.; Weiler, A.; Landenberger, P.; Wahl, F.; Wörth, J.; Scott, L. T.; Gelmont, M.; Olevano, D.; v Issendorff, B. V. Gas-phase production and photoelectron spectroscopy of the smallest fullerene, C20. *Nature* **2000**, *407*, 60−63.

(6) Gao, Z.; Zhang, Z.; Liu, G.; Wang, J.-S. Ultra-low lattice thermal conductivity of monolayer penta-silicene and penta-germanene. *Phys. Chem. Chem. Phys.* **2019**, *21*, 26033−26040.

(7) Zhang, S.; Zhou, J.; Wang, Q.; Jena, P. Beyond Graphitic Carbon Nitride: Nitrogen-Rich Penta-CN_2 Sheet. *J. Phys. Chem. C* **2016**, *120*, 3993−3998.

(8) Li, F.; Tu, K.; Zhang, H.; Chen, Z. Flexible structural and electronic properties of a pentagonal B_2C monolayer via external strain: a computational investigation. *Phys. Chem. Chem. Phys.* **2015**, *17*, 24151−24156.

(9) Laranjeira, J. A. S.; Martins, N. F.; Azevedo, S. A.; Fabris, G. S. L.; Sambrano, J. R. One- and two-dimensional penta-graphene-like structures. *Mater. Today Commun.* **2023**, *35*, 106090.

(10) Oyedele, A. D.; Yang, S.; Liang, L.; Puretzky, A. A.; Wang, K.; Zhang, J.; Yu, P.; Pudasaini, P. R.; Ghosh, A. W.; Liu, Z.; Rouleau, C. M.; Sumpter, B. G.; Chisholm, M. F.; Zhou, W.; Rack, P. D.; Geohegan, D. B.; Xiao, K. $PdSe_2$: Pentagonal Two-Dimensional

Layers with High Air Stability for Electronics. *J. Am. Chem. Soc.* **2017**, *139*, 14090−14097.
(11) Qu, Y.; Kwok, C. T.; Shao, Y.; Shi, X.; Kawazoe, Y.; Pan, H. Pentagonal transition-metal (group X) chalcogenide monolayers: Intrinsic semiconductors for photocatalysis. *Int. J. Hydrogen Energy* **2021**, *46*, 9371−9379.
(12) Wang, L.; Hu, P.; Long, Y.; Liu, Z.; He, X. Recent advances in ternary two-dimensional materials: synthesis, properties and applications. *J. Mater. Chem. A Mater.* **2017**, *5*, 22855−22876.
(13) Zhao, K.; Guo, Y.; Shen, Y.; Wang, Q.; Kawazoe, Y.; Jena, P. Penta-BCN: A New Ternary Pentagonal Monolayer with Intrinsic Piezoelectricity. *J. Phys. Chem. Lett.* **2020**, *11*, 3501−3506.
(14) Varjovi, M. J.; Kilic, M. E.; Durgun, E. Ternary pentagonal BNSi monolayer: Two-dimensional structure with potentially high carrier mobility and strong excitonic effects for photocatalytic applications. *Phys. Rev. Mater.* **2022**, *6*, 034004.
(15) Maymoun, M.; Oukahou, S.; Elomrani, A.; Benaddi, A.; Etrini, A.; Ataalite, H.; Bahou, Y.; Hasnaoui, A.; Sbiaai, K. Potential application of ternary pentagonal p-$SiXY_4$ (X = Si, C, Ge; Y = C, B, N) materials for optoelectronics and photocatalytic water splitting: a first-principles study. *Sustainable Energy Fuels* **2024**, *8*, 1346−1357.
(16) Sharma, S. B.; Qattan, I. A.; Jaishi, M.; Paudyal, D. Penta-SiCN: A Highly Auxetic Monolayer. *ACS Appl. Electron. Mater.* **2022**, *4*, 2561−2569.
(17) Dabsamut, K.; Thanasarnsurapong, T.; Maluangnont, T.; T-Thienprasert, J.; Jungthawan, S.; Boonchun, A. Strain engineering and thermal conductivity of a penta-BCN monolayer: a computational study. *J. Phys. D Appl. Phys.* **2021**, *54*, 355301.
(18) Guo, S.-D.; Wang, S.-Q. Tuning pure out-of-plane piezoelectric effect of penta-graphene: A first-principle study. *J. Phys. Chem. Solids* **2020**, *140*, 109375.
(19) Liu, S.; Liu, B.; Shi, X.; Lv, J.; Niu, S.; Yao, M.; Li, Q.; Liu, R.; Cui, T.; Liu, B. Two-dimensional Penta-BP_5 Sheets: High-stability, Strain-tunable Electronic Structure and Excellent Mechanical Properties. *Sci. Rep.* **2017**, *7* (1), 2404.
(20) Xu, Y.; Ning, Z.; Zhang, H.; Ni, G.; Shao, H.; Peng, B.; Zhang, X.; He, X.; Zhu, Y.; Zhu, H. Anisotropic ultrahigh hole mobility in two-dimensional penta-SiC_2 by strain-engineering: electronic structure and chemical bonding analysis. *RSC Adv.* **2017**, *7*, 45705−45713.
(21) Dovesi, R.; Erba, A.; Orlando, R.; Zicovich-Wilson, C. M.; Civalleri, B.; Maschio, L.; Rérat, M.; Casassa, S.; Baima, J.; Salustro, S.; Kirtman, B. Quantum-mechanical condensed matter simulations with CRYSTAL. *Wiley Interdiscip. Rev.:Comput. Mol. Sci.* **2018**, *8*, No. e1360.
(22) Peintinger, M. F.; Oliveira, D. V.; Bredow, T. Consistent Gaussian basis sets of triple-zeta valence with polarization quality for solid-state calculations. *J. Comput. Chem.* **2013**, *34*, 451−459.
(23) Ferrero, M.; Rérat, M.; Kirtman, B.; Dovesi, R. Calculation of first and second static hyperpolarizabilities of one- to three-dimensional periodic compounds. Implementation in the CRYSTAL code. *J. Chem. Phys.* **2008**, *129*, 244110.
(24) Bader, R. F. W.; Nguyen-Dang, T. T. Quantum Theory of Atoms in Molecules−Dalton Revisited. *Adv. Quantum Chem.* **1981**, *14*, 63−124.
(25) Gatti, C. Chemical bonding in crystals: New directions. *Z. Kristallog.* **2005**, *220*, 399−457.
(26) Wang, V.; Tang, G.; Liu, Y.-C.; Wang, R.-T.; Mizuseki, H.; Kawazoe, Y.; Nara, J.; Geng, W. T. High-Throughput Computational Screening of Two-Dimensional Semiconductors. *J. Phys. Chem. Lett.* **2022**, *13*, 11581−11594.
(27) Grimme, S.; Bannwarth, C.; Shushkov, P. A Robust and Accurate Tight-Binding Quantum Chemical Method for Structures, Vibrational Frequencies, and Noncovalent Interactions of Large Molecular Systems Parametrized for All spd-Block Elements (Z = 1−86). *J. Chem. Theory Comput.* **2017**, *13*, 1989−2009.
(28) Hourahine, B.; Aradi, B.; Blum, V.; Bonafé, F.; Buccheri, A.; Camacho, C.; Cevallos, C.; Deshaye, M. Y.; Dumitrică, T.; Dominguez, A.; Ehlert, S.; Elstner, M.; Van Der Heide, T.; Hermann, J.; Irle, S.; Kranz, J. J.; Köhler, C.; Kowalczyk, T.; Kubař, T.; Lee, I. S.; Lutsker, V.; Maurer, R. J.; Min, S. K.; Mitchell, I.; Negre, C.; Niehaus, T. A.; Niklasson, A. M. N.; Page, A. J.; Pecchia, A.; Penazzi, G.; Persson, M. P.; Řezáč, J.; Sánchez, C. G.; Sternberg, M.; Stöhr, M.; Stuckenberg, F.; Tkatchenko, A.; Yu, V. W.-Z.; Frauenheim, T. DFTB$^+$, a software package for efficient approximate density functional theory based atomistic simulations. *J. Chem. Phys.* **2020**, *152*, 124101.
(29) Bannwarth, C.; Caldeweyher, E.; Ehlert, S.; Hansen, A.; Pracht, P.; Seibert, J.; Spicher, S.; Grimme, S. Extended tight-binding quantum chemistry methods. *Wiley Interdiscip. Rev.:Comput. Mol. Sci.* **2021**, *11*, No. e1493.
(30) Berendsen, H. J. C.; Postma, J. P. M.; Van Gunsteren, W. F.; Dinola, A.; Haak, J. R. Molecular dynamics with coupling to an external bath. *J. Chem. Phys.* **1984**, *81*, 3684−3690.
(31) Wang, V.; Tang, G.; Liu, Y.-C.; Wang, R.-T.; Mizuseki, H.; Kawazoe, Y.; Nara, J.; Geng, W. T. High-Throughput Computational Screening of Two-Dimensional Semiconductors. *J. Phys. Chem. Lett.* **2022**, *13*, 11581−11594.
(32) Espinosa, E.; Alkorta, I.; Elguero, J.; Molins, E. From weak to strong interactions: A comprehensive analysis of the topological and energetic properties of the electron density distribution involving X−H···F−Y systems. *J. Chem. Phys.* **2002**, *117*, 5529−5542.
(33) Macchi, P.; Proserpio, D. M.; Sironi, A. Experimental electron density in a transition metal dimer: Metal-metal and metal-ligand bonds. *J. Am. Chem. Soc.* **1998**, *120*, 13429−13435.
(34) Born, M.; Huang, K.; Lax, M. Dynamical Theory of Crystal Lattices. *Am. J. Phys.* **1955**, *23*, 474.
(35) Ghasemian, M. B.; Daeneke, T.; Shahrbabaki, Z.; Yang, J.; Kalantar-Zadeh, K. Peculiar piezoelectricity of atomically thin planar structures. *Nanoscale* **2020**, *12*, 2875−2901.
(36) Sun, W.; Shen, Y.; Guo, Y.; Chen, Y.; Wang, Q. 1,2,4-Azadiphosphole-based piezoelectric penta-CNP sheet with high spontaneous polarization. *Appl. Surf. Sci.* **2021**, *554*, 149499.
(37) Tang, L.; Cheng, M. Q.; Chen, Q.; Huang, T.; Yang, K.; Huang, W. Q.; Hu, W.; Huang, G. F. Ultrahigh Sensitivity and Selectivity of Pentagonal SiC_2 Monolayer Gas Sensors: The Synergistic Effect of Composition and Structural Topology. *Phys. Status Solidi B* **2020**, *257*, 1900445.
(38) Sharma, S. B.; Qattan, I. A.; Kc, S.; Alsaad, A. M. Large Negative Poisson's Ratio and Anisotropic Mechanics in New Penta-PBN Monolayer. *ACS Omega* **2022**, *7*, 36235−36243.
(39) Djamel, B.; Haidar, E.-A.; Stampfl, C.; Naouel, C.; Ali, M.; Sahnoun, M. Strain Engineering of the Pentagonal PtSiTe Monolayer for Enhanced Photovoltaic and Thermoelectric Efficiency: A First-Principles Investigation. *ACS Appl. Nano Mater.* **2023**, *7*, 142−152.
(40) Morshedi, H.; Naseri, M.; Hantehzadeh, M. R.; Elahi, S. M. Theoretical Prediction of an Antimony-Silicon Monolayer (penta-Sb_2Si): Band Gap Engineering by Strain Effect. *J. Electron. Mater.* **2018**, *47*, 2290−2297.
(41) Naseri, M.; Lin, S.; Jalilian, J.; Gu, J.; Chen, Z. Penta-P2X (X = C, Si) monolayers as wide-bandgap semiconductors: A first principles prediction. *Front. Phys.* **2018**, *13*, 138102.
(42) Ribag, K.; Houmad, M.; Laamara, R. A.; Benyoussef, A.; El Kenz, A. Strain enhances the electrical and photocatalytic properties of tetragonal boron nitride. *Optik* **2023**, *283*, 170872.
(43) Martins, N.; Laranjeira, J. A. S.; de Azevedo, S.; Sambrano, J. Strain Engineering to Improve the Electronic and Photocatalytic Properties of the Inorganic Graphenylene Based on SiC. *ACS Appl. Electron. Mater.* **2024**, *6*, 2700−2708.
(44) Laranjeira, J. A. S.; Silva, J. F.; Denis, P. A.; Maia, A. S.; Sambrano, J. R. Novel buckled graphenylene-like InN and its strain engineering effects. *Comput. Theor. Chem.* **2024**, *1231*, 114418.
(45) Luo, M.; Xu, Y. E. Tunable band-gap of the GeC monolayer by strain and electric field: A first-principles study. *Optik* **2019**, *195*, 163147.
(46) Behera, H.; Mukhopadhyay, G. Tailoring the structural and electronic properties of a graphene-like ZnS monolayer using biaxial strain. *J. Phys. D Appl. Phys.* **2014**, *47*, 075302.

(47) Guo, S.-D.; Mu, W.-Q.; Zhu, Y.-T. Biaxial strain enhanced piezoelectric properties in monolayer g-C_3N_4. *J. Phys. Chem. Solids* **2021**, *151*, 109896.
(48) Guo, S.-D.; Guo, X.-S.; Liu, Z.-Y.; Quan, Y.-N. Large piezoelectric coefficients combined with high electron mobilities in Janus monolayer XTeI (X = Sb and Bi): A first-principles study. *J. Appl. Phys.* **2020**, *127*, 064302.
(49) Cook, T. R.; Dogutan, D. K.; Reece, S. Y.; Surendranath, Y.; Teets, T. S.; Nocera, D. G. Solar energy supply and storage for the legacy and nonlegacy worlds. *Chem. Rev.* **2010**, *110*, 6474−6502.
(50) Zhang, P.; Zhang, J.; Gong, J. Tantalum-based semiconductors for solar water splitting. *Chem. Soc. Rev.* **2014**, *43*, 4395−4422.
(51) Wang, J.; Sun, H.; Huang, J.; Li, Q.; Yang, J. Band structure tuning of TiO_2 for enhanced photoelectrochemical water splitting. *J. Phys. Chem. C* **2014**, *118*, 7451−7457.
(52) Kudo, A.; Miseki, Y. Heterogeneous photocatalyst materials for water splitting. *Chem. Soc. Rev.* **2009**, *38*, 253−278.
(53) Chowdhury, C.; Karmakar, S.; Datta, A. Monolayer Group IV-VI Monochalcogenides: Low-Dimensional Materials for Photocatalytic Water Splitting. *J. Phys. Chem. C* **2017**, *121*, 7615−7624.
(54) Wang, N.; Li, X.; Wang, Y.; Quan, X.; Chen, G. Evaluation of bias potential enhanced photocatalytic degradation of 4-chlorophenol with TiO_2 nanotube fabricated by anodic oxidation method. *Chem. Eng. J.* **2009**, *146*, 30−35.

https://doi.org/10.1021/acsphyschemau.4c00068
ACS Phys. Chem Au 2025, 5, 62−71